Pergamon

Int. J. Heat Mass Transfer. Vol. 39, No. 10, pp. 2039–2051, 1996

0017–9310/96 $15.00 + 0.00

0017–9310(95)00302–9

Multi-zone simulation of the Bridgman growth process of β-NiAl crystal

HONG OUYANG and WEI SHYY†

Department of Aerospace Engineering, Mechanics and Engineering Science, University of Florida, Gainesville, FL 32611, U.S.A.

(*Received* 6 *February* 1995 *and in final form* 31 *July* 1995)

Abstract—A computational model has been developed for the Bridgman growth process of β-NiAl crystal. The model accounts for heat transfer in the whole furnace system, including the encapsulated fluid between the heater and the ampoule, conjugate heat transfer around and within the ampoule, and phase change dynamics between melt and crystal. To handle the geometrical and physical complexities of the crystal growth processes, a two-level approach has been developed. At the global furnace level, combined convection/conduction/radiation calculations with realistic geometrical and thermal boundary conditions are made inside the whole system. Refined calculations are then made within the ampoule, with the boundary conditions supplied by the global furnace simulations. The present multi-level model can help improve the predictive capabilities for crystal growth techniques by optimizing the use of the computing resources; it allows one to probe the effects of different physical and geometrical variables on the crystal quality.

1. INTRODUCTION

β-NiAl is an intermetallic that is currently being investigated as a promising high temperature structural material for application in the next generation of aircraft engines and structural components. NiAl is especially attractive because of its low density, high thermal conductivity, high melting temperature, superior isothermal and cyclic oxidation resistance [1]. However, it has two major drawbacks; low toughness at room temperatures and low strength at high temperatures [2]. These deficiencies need to be resolved before NiAl can be used in structural applications. The current study is part of an ongoing effort to grow high purity single crystals of NiAl with controlled compositions and under controlled conditions. This would be the starting point in fundamental and detailed studies directed towards understanding the behavior of this material.

The Bridgman growth system is one of the directional solidification configurations that are useful for producing large size single crystals from the melt [3]. The advantage of the Bridgman system is that the temperature gradients can be controlled, making it possible to achieve unidirectional solidification. This study is directed towards the prediction of the thermal characteristics of a Bridgman growth system that has and is currently being used to produce single crystals of NiAl. A schematic of the growth system is shown in Fig. 1.

The temperature distribution in crystal growth systems, such as the Bridgman system, is highly complex and is influenced by several factors such as varying thermo-physical properties and multiple heat transfer modes, namely, conduction, convection and radiation. These complications have traditionally resulted in simplified analyses carried out under quite restrictive assumptions of simplified geometry, assumed boundary conditions, constant thermophysical properties and neglecting important convection modes such as buoyancy driven convection. Our general understanding of the transport process and macroscopic properties of the crystal growth during the last three decades has improved substantially. However, quantitative prediction of the performance of specific crystal growth devices is not yet feasible. Efforts have been made in the research community to develop such predictive capabilities. For example, Brown [4] reviewed calculations, conducted by his research group using the finite element method, of the temperature field in the melt, crystal, and ampoule, the location of melt/crystal and melt/ambient surfaces during crystal growth. Shyy [5] previewed many of the possible factors that contribute to the solidification and heat transport, such as natural convection, Marangoni convection, solute concentration, turbulence and capillarity, at both macroscopic and morphological scales. In all these aspects, active investigations are being made to address the issues of the interfacial dynamics in conjunction with the macroscopic solute segregation and melt oscillation [5–7], and microscopic morphological evolution [5, 8–10]. In this study we have attempted to realistically model the system taking into account complex geometry,

† Author to whom correspondence should be addressed.

NOMENCLATURE

A	permeability coefficient
C_p	specific heat
f	fluid fraction
f_c	ratio of distances between points E–e and between points e–P, used for harmonic interpolation
g	gravitational acceleration
H	ampoule position within the furnace
ΔH_0	latent heat of NiAl
k	thermal conductivity
P	dimensionless pressure
Pr_0	Prandtl number based on NiAl properties at 300 K
q	radiation heat flux between ampoule outer wall and heater
R_0	reference length scale based on ampoule inner radius
Ra_0	Rayleigh number based on NiAl properties at 300 K
r	dimensionless radial coordinate
r_a	radial position of the ampoule outer wall
r_h	radial position of the heater
St_0	Stefan number based on NiAl properties at 300 K
Su	source term accounting for phase change in the radial momentum equation
Sw	source term accounting for phase change in the axial momentum equation
t	dimensionless time
T	dimensionless temperature
$T1$	cooler temperature
$T4$	heater temperature
T_a	temperature of the ampoule outer wall
T_h	temperature of the heater, $T_h = T4$
ΔT	reference temperature scale, $\Delta T = T4 - T1$
u	dimensionless radial velocity
w	dimensionless axial velocity
z	dimensionless axial coordinate.

Greek symbols

α	thermal diffusivity
β	thermal expansion coefficient
ε_a	emissivity of the ampoule outer wall
ε_h	emissivity of the heater
μ	viscosity
ϱ	density
σ	Stefan–Boltzmann constant, 5.67×10^{-8} [W m^{-2} k^{-4}].

Subscripts

E	node index of the east unknown control volume E
P	node index of the present unknown control volume P
e	east surface of the present control volume P
a	ampoule
h	heater
0	reference scale.

temperature and phase dependent material properties, buoyancy driven convection and its influence on the melt/crystal interface and the thermal distribution within the crystal.

In the following, we first formulate the physical phenomena that is involved in this Bridgman growth process for β-NiAl, then develop the numerical strategy to solve this problem, and finally present the simulation results and the corresponding findings.

2. FORMULATION AND COMPUTATIONAL STRATEGY

Figure 1 shows the schematic of a practical designed vertical Bridgman furnace for growing β-NiAl [11] that we chose for our current numerical simulation. For the purposes of our calculation, the furnace is composed of two parts:

(i) the enclosure, filled with argon, containing the heater ($T4$) and;

(ii) the axisymmetric ampoule containing the melt, the growing crystal and the cooler ($T1$).

The ampoule is made of alumina and rests on a copper support. The enclosure stays stationary during the growth process and the ampoule is pulled out to control the growth speed of the crystal.

The following phenomena are of key importance and need to be resolved adequately:

- melt/crystal phase change in the ampoule region;
- conduction among various components of the furnace, the alumina wall and the copper base;
- convection in the melt and the encapsulated gas argon;
- radiation between the heater $T4$ and the ampoule wall.

(i) *Governing equations*

To formulate this problem with combined heat transfer and phase change in a geometrically complex

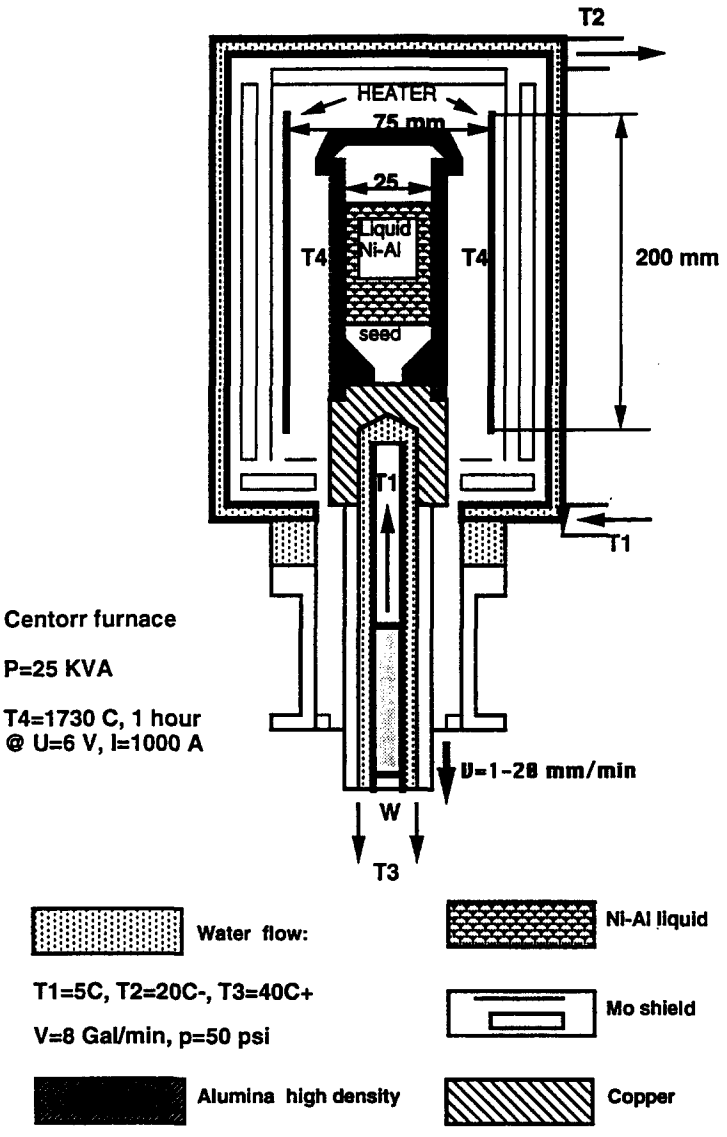

Fig. 1. Schematic of vertical Bridgman growth furnace for growing β-NiAl.

domain, we have derived and solved a set of unified governing equations that describes the conduction, convection and phase change phenomena over the entire geometry of the system. The dimensionless, axisymmetric, Navier–Stokes and energy equations, incorporating variable thermal conductivities and the Boussinesq approximation are:

(i) Continuity equation

$$\frac{\partial}{\partial r}\left(\frac{\varrho}{\varrho_0}ru\right)+\frac{\partial}{\partial z}\left(\frac{\varrho}{\varrho_0}rw\right)=0, \tag{1}$$

where u and w are, respectively, the velocity components along the radial and axial direction.

(ii) Momentum equation

r-momentum:

$$\frac{\partial}{\partial t}\left(\frac{\varrho}{\varrho_0}ru\right)+\frac{\partial}{\partial r}\left(\frac{\varrho}{\varrho_0}ruu\right)+\frac{\partial}{\partial z}\left(\frac{\varrho}{\varrho_0}rwu\right)=-r\frac{\partial P}{\partial r}$$
$$+Pr_0\left\{\frac{\partial}{\partial r}\left(\frac{\mu}{\mu_0}r\frac{\partial u}{\partial r}\right)+\frac{\partial}{\partial z}\left(\frac{\mu}{\mu_0}r\frac{\partial u}{\partial z}\right)\right\}-Pr_0\left(\frac{\mu}{\mu_0}\right)\frac{u}{r}+Su. \tag{2}$$

z-momentum:

$$\frac{\partial}{\partial t}\left(\frac{\varrho}{\varrho_0}rw\right)+\frac{\partial}{\partial r}\left(\frac{\varrho}{\varrho_0}ruw\right)+\frac{\partial}{\partial z}\left(\frac{\varrho}{\varrho_0}rww\right)$$
$$=-r\frac{\partial P}{\partial z}+Pr_0\left\{\frac{\partial}{\partial r}\left(\frac{\mu}{\mu_0}r\frac{\partial w}{\partial r}\right)+\frac{\partial}{\partial z}\left(\frac{\mu}{\mu_0}r\frac{\partial w}{\partial z}\right)\right\}$$
$$+Ra_0Pr_0\left(\frac{\varrho}{\varrho_0}\right)\left(\frac{\beta}{\beta_0}\right)rT+Sw. \tag{3}$$

Table 1. Thermodynamic and transport properties

Material	ϱ (kg m^{-3})	μ (kg m^{-1} s^{-1})	k (W m^{-1} K^{-1})	C_p (J kg^{-1} K^{-1})	β (K^{-1})
NiAl	5950	0.005	75	660	1.52×10^{-5}
Argon	0.487	5.42×10^{-5}	0.0427	520	8.33×10^{-4}
Alumina	3975	†	‡	765	—
Copper	8930	†	‡	386	—

$\Delta H_0 = 688$ kJ kg^{-1}.
† Assigned big values.
‡ Varied with temperature (see Fig. 4).

(iii) Energy equation

$$\left\{\frac{\partial}{\partial t}\left(\frac{\varrho}{\varrho_0}\frac{Cp}{Cp_0}rT\right)+\frac{\partial}{\partial r}\left(\frac{\varrho}{\varrho_0}\frac{Cp}{Cp_0}ruT\right)+\frac{\partial}{\partial z}\left(\frac{\varrho}{\varrho_0}\frac{Cp}{Cp_0}rwT\right)\right\}$$
$$=\left\{\frac{\partial}{\partial r}\left(\frac{k}{k_0}r\frac{\partial T}{\partial r}\right)+\frac{\partial}{\partial z}\left(\frac{k}{k_0}r\frac{\partial T}{\partial z}\right)\right\}$$
$$-\frac{1}{St_0}\left\{\frac{\partial}{\partial t}\left(\frac{\varrho}{\varrho_0}rf\right)+\frac{\partial}{\partial r}\left(\frac{\varrho}{\varrho_0}ruf\right)+\frac{\partial}{\partial z}\left(\frac{\varrho}{\varrho_0}rwf\right)\right\}, \quad (4)$$

where the term with Ra_0 in equation (3) comes from the Boussinesq approximation for treating the buoyancy effect, Su, Sw in equations (2) and (3) and the terms with fluid fraction f in equation (4) are appropriate source terms to account for the phase change, ϱ, μ, Cp, k and β are the density, viscosity, specific heat, conductivity and coefficient of thermal expansion, respectively. Ra_0, Pr_0 and St_0 are the Rayleigh number, Prandtl number and Stefan number, respectively. Their definitions are

$$Ra_0 = \frac{\text{Buoyancy force}}{\text{Viscous force}} = \frac{\varrho_0 g\beta_0 \Delta T R_0^3}{\alpha_0\mu_0} \quad (5)$$

$$Pr_0 = \frac{\text{Kinematic viscosity}}{\text{Heat diffusivity}} = \frac{\mu_0/\varrho_0}{\alpha_0} \quad (6)$$

$$St_0 = \frac{\text{Sensible heat}}{\text{Latent heat}} = \frac{Cp_0\Delta T}{\Delta H_0}, \quad (7)$$

where α_0, ϱ_0, μ_0, Cp_0, k_0 and β_0 are chosen reference material properties for nondimensionalization. g is gravitational acceleration, ΔH_0 is the reference latent heat, R_0 is the reference length, and ΔT is the reference temperature. In this study, we chose the properties of β-NiAl at 300 K as the reference properties, the radius of ampoule inner wall R_0 as the reference length and the difference between the highest and the lowest temperature in the furnace, $\Delta T = T4 - T1$, as the reference temperature scale. The estimated dimensionless parameters for our current calculation are

$$Ra_0 = 3.2\times10^4 \quad Pr_0 = 4.4\times10^{-2} \quad St_0 = 1.7. \quad (8)$$

Furthermore, the original parameters of the material properties for different material regions, which have been listed in Table 1, are converted correspondingly into dimensionless form as listed in Table 2.

(ii) Two-level modeling strategy

It may be observed from Fig. 1 that the combination of the furnace enclosure and the ampoule presents a very complicated geometry. To render the computations tractable and simultaneously obtain adequate resolution in the ampoule region, a two-level strategy is employed. Level 1 simulates the entire domain and is referred to as the global furnace model. Level 2 concentrates on the ampoule region and obtains its boundary conditions from the level 1 or the global simulation. With this two-level strategy, we can obtain useful information at the global level and yet obtain adequate resolution at the melt/crystal interface. Figure 2 demonstrates the application of the two-level strategy to the present simulation. To solve the governing equations, the control volume technique employing a non-orthogonal body-fitted coordinate system has been adopted [5, 12, 13]. A proven and robust pressure-based algorithm is then used to iterate the discretized form of the governing equations to the steady state [12, 14].

Table 2. Dimensionless thermodynamic and transport properties

Material	ϱ/ϱ_0	$Pr_0(\mu/\mu_0)$	k/k_0	C_p/C_{p0}	$Ra_0/Pr_0(\beta/\beta_0)(\varrho/\varrho_0)$
NiAl	1.0	4.4×10^{-2}	1.0	1.0	1.4×10^3
Argon	8.2×10^{-5}	4.77×10^{-5}	5.7×10^{-4}	0.79	6.32
Alumina	0.67	†	‡	1.16	—
Copper	1.5	†	‡	0.58	—

† Assigned big values.
‡ Varied with temperature (see Fig. 4).

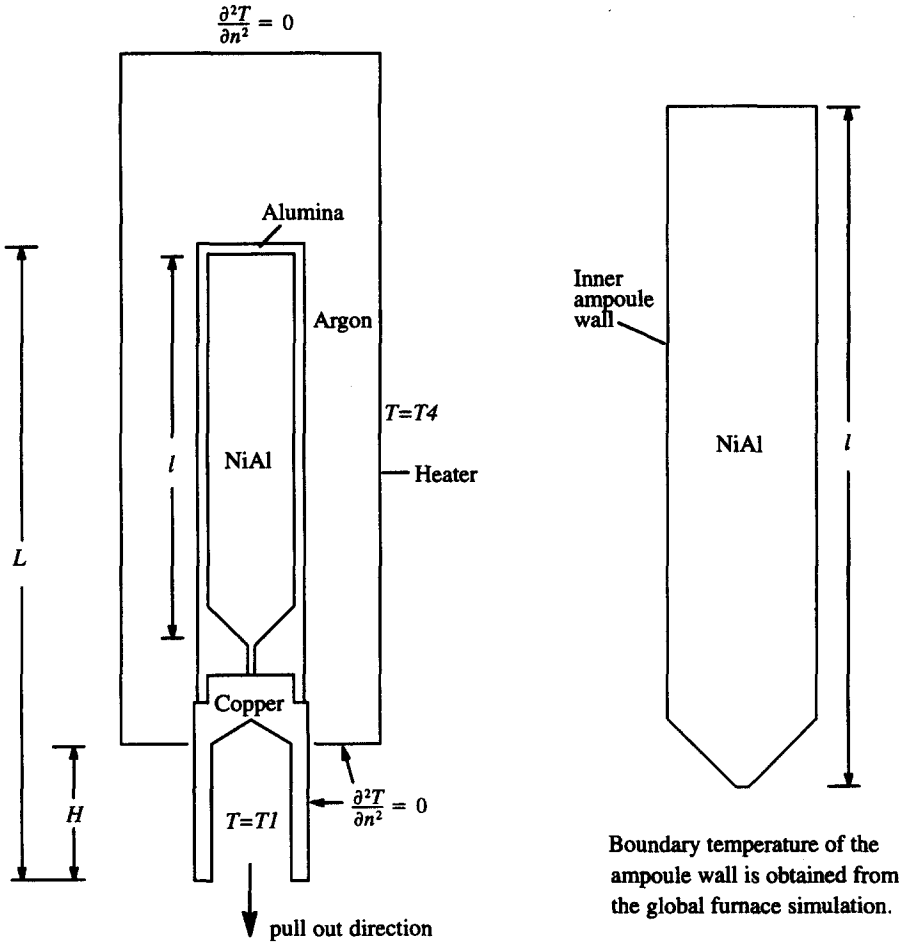

Fig. 2. Layout and boundary conditions for (a) the global furnace model, and (b) the refined ampoule model used in the present numerical simulation, where H measures the ampoule position as it is pulled out. The total length of the ampoule part, between the top of alumina and the bottom of copper, is L = 185 mm, while the length of the ampoule is l = 113.5 mm.

(iii) The treatment of phase change

In the modeling of the melt/solid interface region, phase change needs to be considered along with the coupled mass and heat transport. Special treatment thus need to be taken to account for the release of latent heat during solidification [5, 15, 16]. As is shown in equation (4), an enthalpy based method has been adopted in the energy equation through the implementation of the fluid fraction f in the source term. Here, f is defined to be 1 in the region of melt, zero in the region of solid, and varies continuously between zero and unity when the material undergoes phase change. In addition, Su and Sw are included in the momentum equations (2) and (3) to enforce the velocity in the solid to match the pull rate of the crystal. The approach taken here is the inclusion of Darcy-type source terms in the momentum equations [5, 15]. Thus the phase change material in the solid/melt interface region is considered to be a porous medium, with the porosity changing from zero to unity as the material melts. For pure materials, the porosity changes abruptly as the phase change occurs, but to ensure numerical stability, a continuous variation is imposed. Here, the source terms have the form: $Su = -Au$ and $Sw = -Aw$, where A varies as a function of the fluid fraction f from zero in the liquid phase to infinity in the solid phase [15, 17].

(iv) The interpolation of material properties

The calculations conducted in this study take into account the variation of material properties with temperature, such as thermal conductivity, at the ampoule walls and at the melt/crystal interface. Abrupt changes in material properties may be expected at the interfaces between two media and the interpolation for the material properties must be handled carefully in order to obtain numerical solutions. The usual approach taken is linear interpolation,

$$k_c = f_c k_P + (1 - f_c) k_E, \tag{9}$$

where f_e designates the ratio of distances between points E–e and between points e–P, with E, P, and e representing, respectively, the east-side unknown node, the present unknown node, and the east-side control surface of the present unknown cell P. Here, a standard arithmetic averaging with $f_e = 0.5$ is chosen for interpolation within the same material media. However, this does not handle abrupt changes at the interface between the two media. Hence, following Patankar [14], a harmonic interpolation based on a one-dimensional flux conservation is used as follows:

$$k_e = \frac{1}{(1-f_e)/k_P + f_e/k_E}. \tag{10}$$

This treatment has been compared with the flux balance approach [18] and is found to be equally robust and accurate; but simpler to implement.

(*v*) *Radiation effect*

The radiation heat flux between the heat ($T4$) and the outer wall of the ampoule is handled by the following simplified treatment [19]:

$$q = \frac{\sigma(T_a^4 - T_h^4)}{(1/\varepsilon_a) + \left(\frac{1-\varepsilon_h}{\varepsilon_h}\right)(r_a/r_h)}, \tag{11}$$

where $\sigma = 5.67 \times 10^{-8}$ W m^{-2} K^4 is the Stefan–Boltzmann constant, T_a, r_a, and ε_a are temperature, radial position and emissivity for the ampoule outer wall and T_h, r_h and ε_n are the corresponding variables for the heater. The heater is considered to be a black body, so $\varepsilon_h = 1.0$. For the alumina wall of the ampoule, $\varepsilon_a = 0.8$ and for the copper wall, $\varepsilon_a = 0.6$. The expression for the boundary condition at the outer ampoule wall is given by,

$$-k\frac{\partial T}{\partial r}\bigg|_{\text{ampoule}} = -k\frac{\partial T}{\partial r}\bigg|_{\text{argon}} + q, \tag{12}$$

where the left hand side represents the heat flux into the ampoule wall and the right hand side represents the heat flux due to convection and conduction from the encapsulating gas and the radiation from the heater.

3. RESULTS AND DISCUSSION

In the following, we present the results of steady state calculations for the Bridgman growth of NiAl. The geometry of the calculation domain is shown in Fig. 2a, b. In order to optimize computational costs without sacrificing accuracy and resolution in the melt/crystal region, the simulation was conducted at two levels. Level 1 is the global furnace simulation involving the entire domain. Level 2 is a refined ampoule simulation and takes its boundary conditions based on the global simulation. It will be shown later that the global simulation is relatively insensitive to the details of the interface morphology. We also try to take into account the relative displacement of the ampoule as the growing crystal is pulled out of the furnace. Therefore, three simulations have been performed at the global level involving three different locations of the ampoule. A multi-zone patched grid method has been employed to generate the grid system needed for global (furnace) level simulations. Sample grid distributions have been shown in Fig. 3a, b for $H = 40$ and 80 mm, where H indicates the position of the ampoule within the furnace. The global furnace (Level 1) simulations were conducted for three different ampoule positions in order to estimate the effects of geometric variations as the crystal is pulled out of the furnace. Calculations were conducted for $H = 40$ mm (151×213 grid), 80 mm (151×216 grid) and 120 mm (151×219 grid). In all cases, there were 51×103 points in the ampoule region. Based on this resolution, the ampoule region is then computed again with a better resolution; the boundary conditions needed for this Level 2 simulation are extracted from the results obtained from the Level 1 solutions. In the following sections, we will first show that consideration of realistic material property variation, as, e.g. functions of temperature, is essential to obtain a faithful simulation; we will then discuss the solutions obtained for different ampoule locations on both Level 1 and Level 2.

(*i*) *The global furnace simulation*

Figure 4 shows the variation of thermal conductivity of alumina and copper with temperature [20]. Figures 5 and 6 show the stream function and the isotherm distribution, respectively, for each of the three ampoule locations. The streamline pattern arises as a result of buoyancy driven convection. It may be observed that the convection pattern in the encapsulating gas is quite weak and the convective heat transfer into the ampoule is negligible compared to the radiative effect from the heater. As the ampoule translates downward, the convection within the ampoule gets slightly weaker and the melt/crystal interface becomes convex towards the melt. It is difficult to predict the strength and detailed characteristics of the convective field within the furnace because the geometry is complicated and the boundary conditions vary with the ampoule movement. Nevertheless, it is clear that the isotherm pattern changes quite significantly as the crystal is drawn down and the temperature gradients at the base of the crystal decrease in magnitude. To shed some light on the role played by the variations of the transport properties, with respect to temperature, calculations have also been conducted with the material properties held fixed to the reference values at 300 K, a practice employed in some modeling work. While the general patterns of stream functions and isotherms seem insensitive, some critical aspects of the solutions are substantially affected. As an illustration, Fig. 7 shows the differences in the temperature distribution along the centerline and

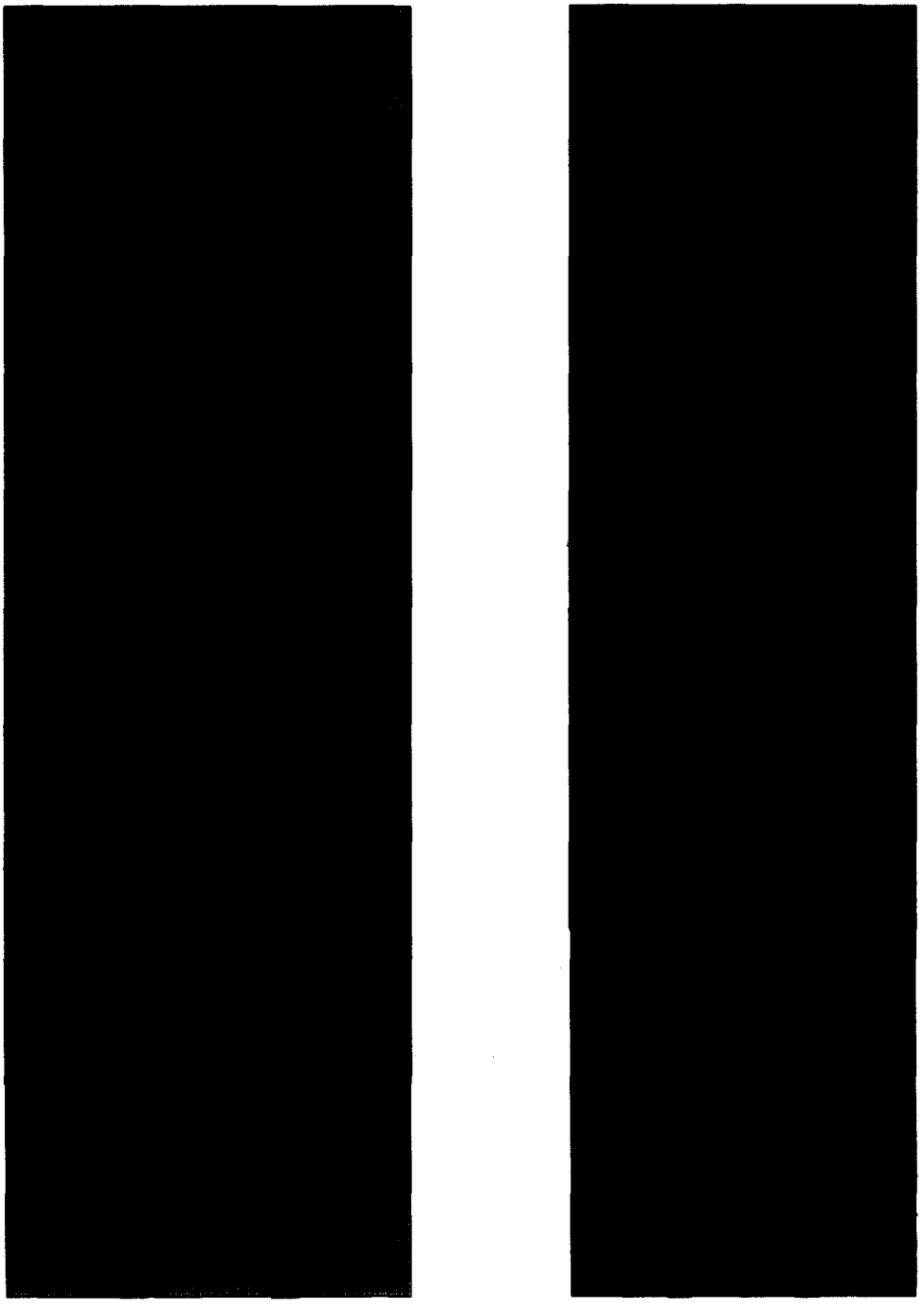

(a) Grid of H=40mm *(b) Grid of H=80mm*

Fig. 3. Grid distributions for the global furnace model of (a) $H = 40$ mm (grid size = 151×213), and (b) $H = 80$ mm (grid size = 151×216).

the inner wall of the ampoule, between the variable properties and constant properties simulations. Noticeable differences have been observed; for example, a 50% difference exists along the bottom wall of the ampoule. The differences exhibited in Fig. 7 impact the temperature distribution in the crystal and its accurate prediction is necessary to understand its implications on crystal quality.

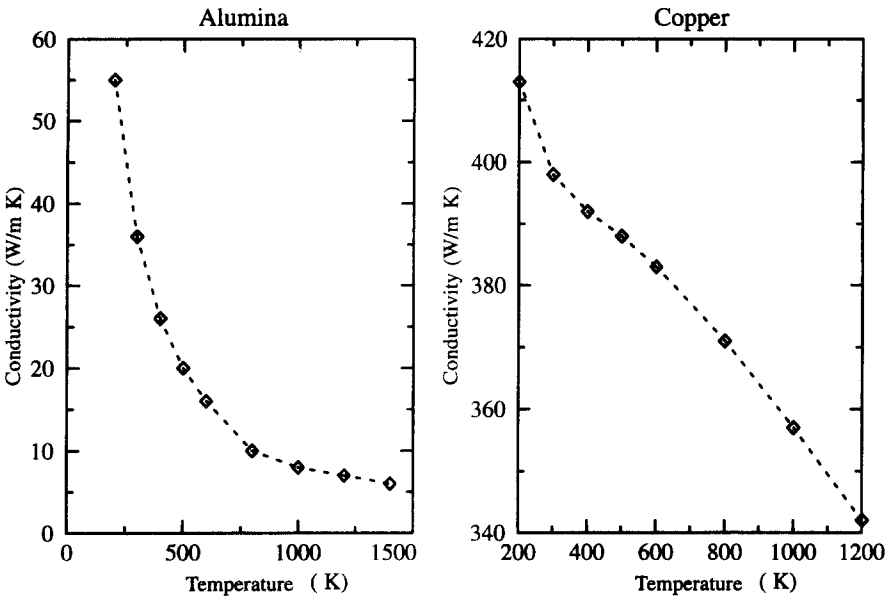

Fig. 4. Dependency of thermal conductivities of alumina and copper on temperature (*Perry's Chemical Engineerings' Handbook*, 1984).

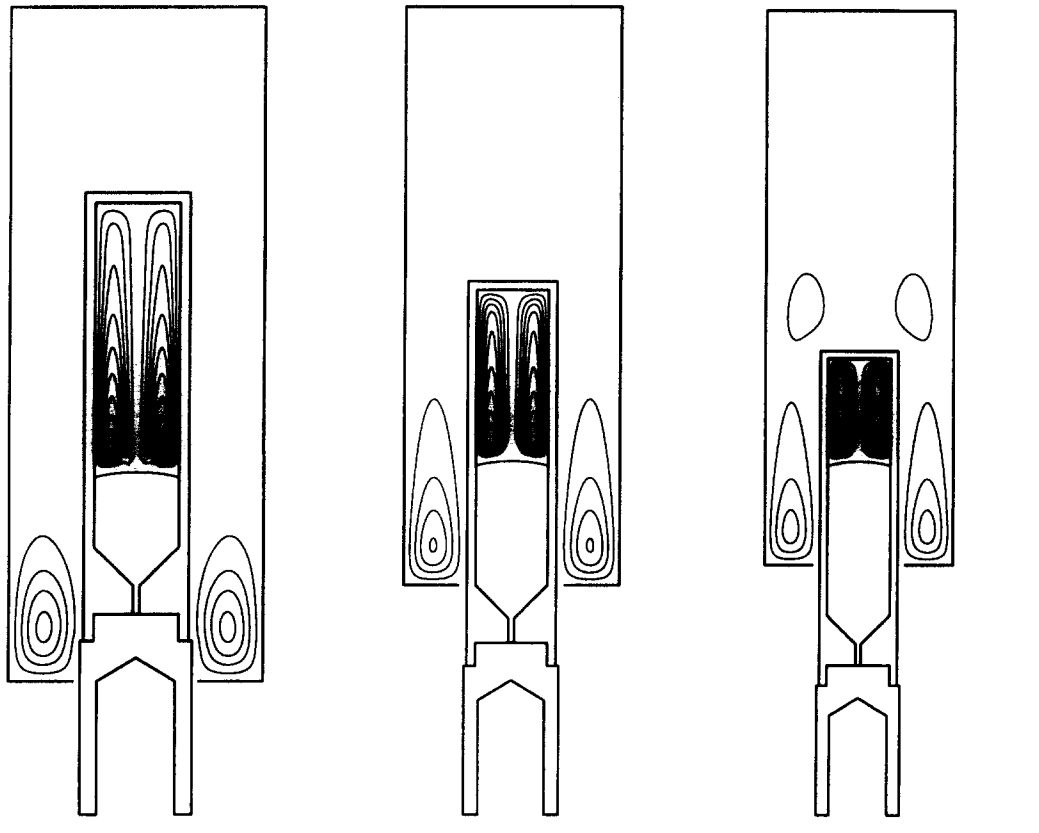

Fig. 5. Solution characteristics of the global furnace simulation for three different H. (i) $H = 40$ mm; (ii) $H = 80$ mm; (iii) $H = 120$ mm. Stream function.

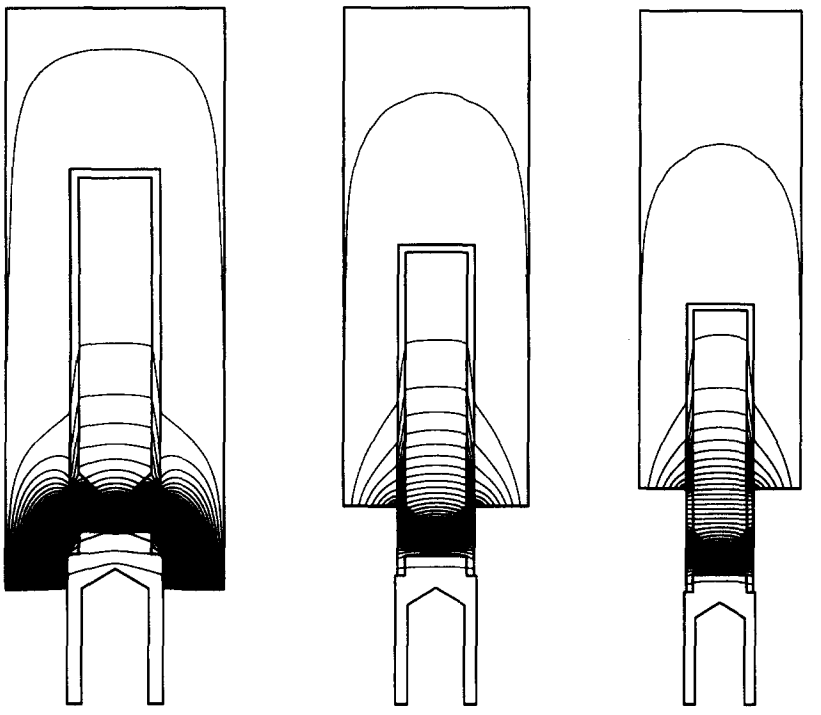

Fig. 6. Solution characteristics of the global furnace simulation for three different H. (i) $H = 40$ mm; (ii) $H = 80$ mm; (iii) $H = 120$ mm. Isotherms.

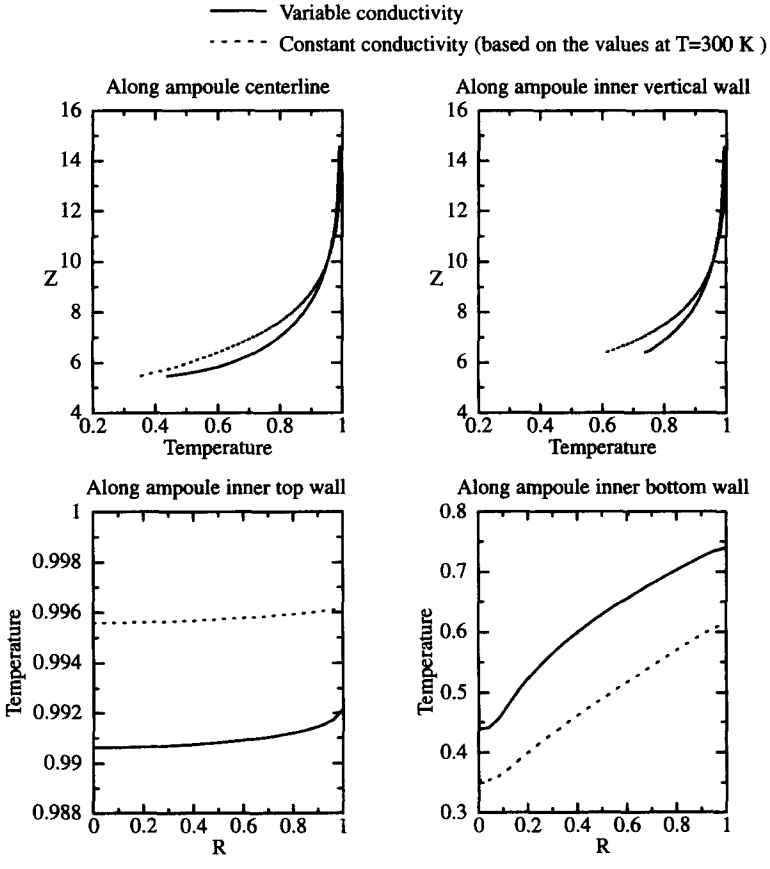

Fig. 7. Comparison of the temperature profiles of the global furnace model with variable and constant thermal conductivities of alumina and copper for $H = 80$ mm.

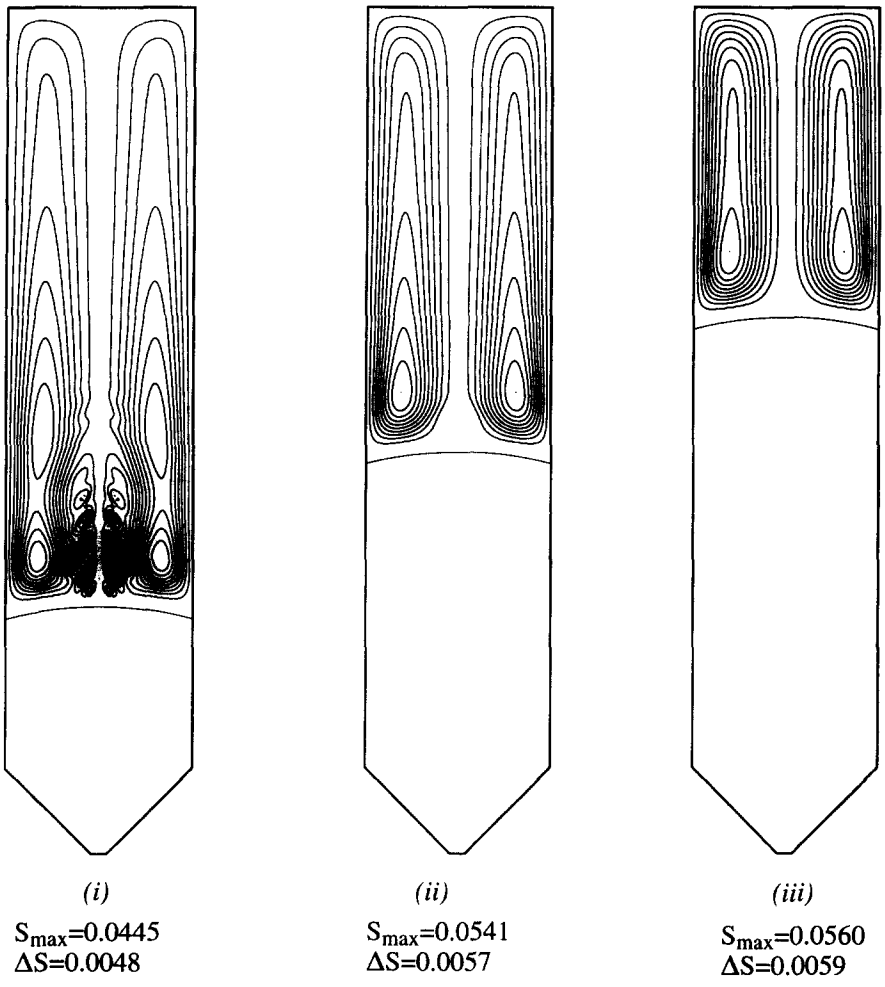

Fig. 8. Solution characteristics of the refined ampoule simulation for three different H. (i) $H = 40$ mm; (ii) $H = 80$ mm; (iii) $H = 120$ mm. Stream function.

(ii) The refined ampoule simulation

The refined ampoule (Level 2) simulation was conducted using the ampoule wall temperature distribution, obtained from Level 1, as the boundary condition. The grid resolution within the ampoule has been increased to 101×154 from 51×103 used at Level 1. Stream function and isotherm contours are presented in Figs. 8 and 9, respectively. Noticeable differences may be observed between the convection patterns in Fig. 5(i–iii) and Fig. 8(i–iii), and more significantly, the convection strengths are different, especially for $H = 40$ mm. At this ampoule position, the more detailed secondary vortical structure in the central region above the solid–melt interface can be clearly observed from the refined solutions depicted in Fig. 8; at the global level, as shown in Fig. 5, such characteristics are less pronounced. This assessment shows that a fine grid is needed to capture convection dominated phenomena, thus justifying the two level approach taken in this study.

Figure 10 contrasts the melt/crystal interface obtained from the two level simulation for all three ampoule locations. It may be observed that the differences between the coarse grid (Level 1) and the fine grid (Level 2) calculations are most significant when the melt volume decreases (as the crystal is pulled out). This observation just reinforces the trends exhibited in the stream function plots mentioned previously. The sensitivity to grid refinement increases as the melt volume decreases because of the constraining effect of the top wall. Since the interface positions at the ampoule wall are the same between the two grid levels, it is significant that the temperature distributions predicted on them are different, resulting in different melt/crystal curvatures. This aspect impacts on the detailed distribution of temperature gradients in the interface region, resulting in a different micro-structure of the crystal.

To further illustrate the usefulness of the multi-level approach, a fine grid simulation of the $H = 40$ mm case, corresponding to Fig. 5(i) and Fig. 6(i), was carried on a refined grid of 223×284 nodes (73×154 nodes in the ampoule region). This represents a substantial refinement over the grid system shown in Fig.

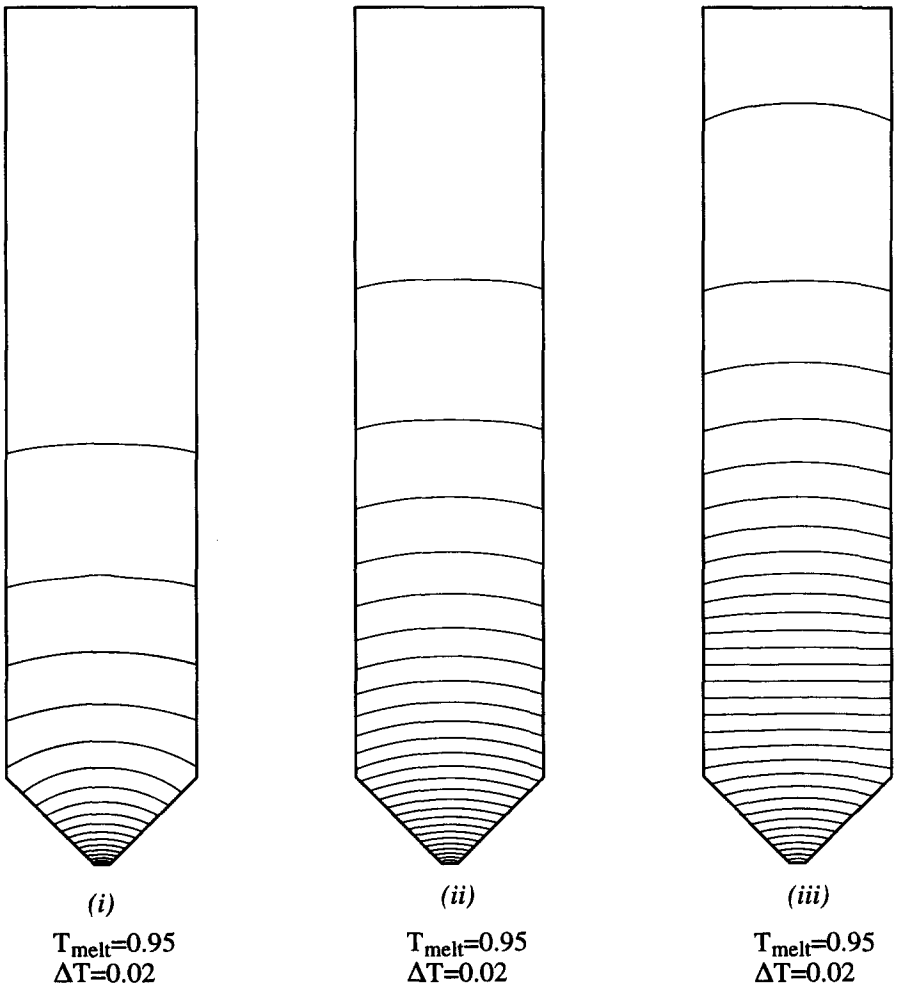

Fig. 9. Solution characteristics of the refined ampoule simulation for three different H. (i) $H = 40$ mm; (ii) H 80 mm; (iii) $H = 120$ mm. Isotherms.

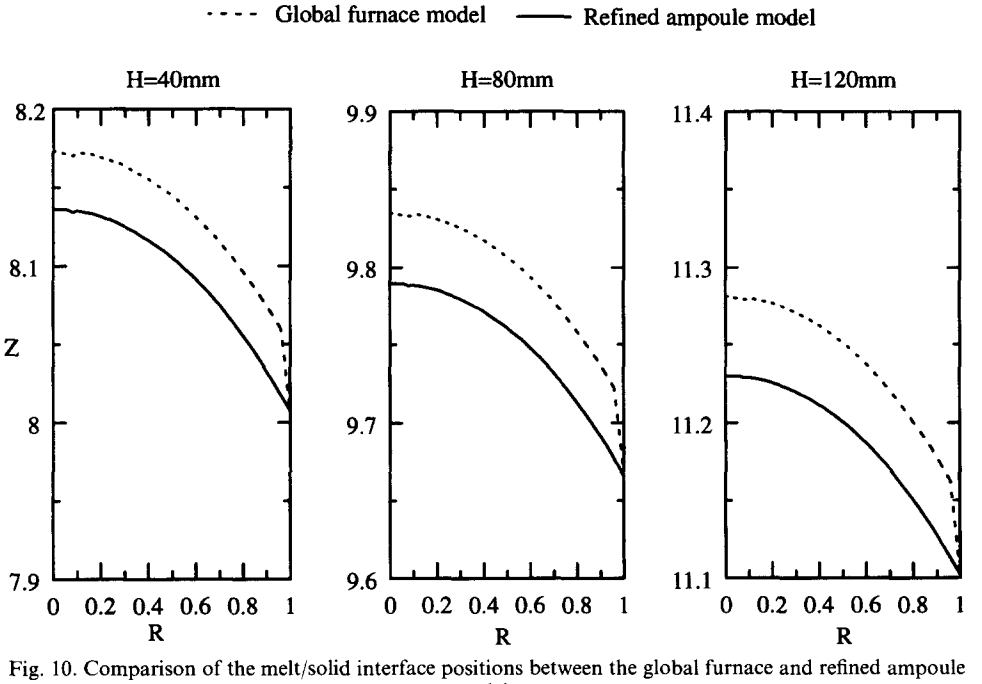

Fig. 10. Comparison of the melt/solid interface positions between the global furnace and refined ampoule models.

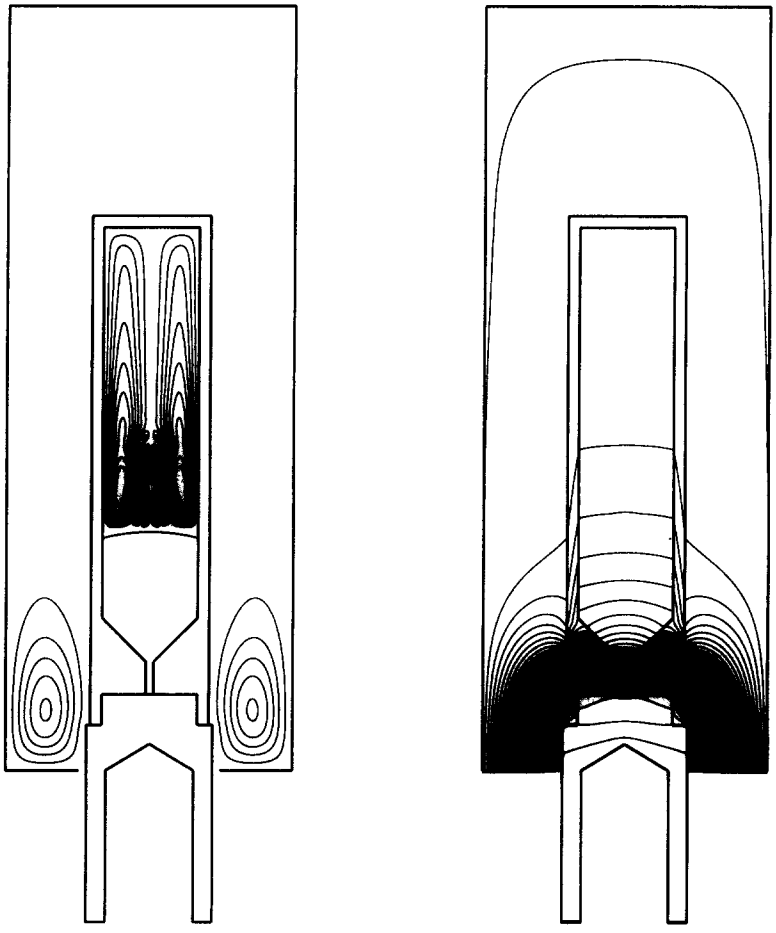

Fig. 11. Solution characteristics of the global furnace simulation for $H = 40$ mm with grid size: 223×284.

3a with 151×213 nodes (51×103 nodes in the ampoule region). Figure 11(i) and (ii) show the streamfunction and isotherms, respectively, obtained on this fine grid system. It can be observed that the fine grid solution captures more details of the convection pattern within the ampoule. Differences can be noted between the solutions presented in Figs. 5 and 6 and those presented in Fig. 11; more secondary vortical structures are captured on the fine grid. The fine grid solution is closer to the refined ampoule simulation (Figs. 8 and 9) than to the coarse grid solutions from the global furnace simulation. The fine grid results of the global furnace simulation clearly demonstrate the economy of the multi-level approach; instead of resorting to a fine grid distribution at the global level, carrying out the refined ampoule simulation yields the desired accuracy economically.

Correlations between the thermal characteristics in the combined crystal/melt region and the microscopic structure of NiAl are not well established at the present time. However, the capability established in this work to predict the solidification dynamics and thermal field will aid the development of such critical information.

4. CONCLUSION

Accurate and realistic numerical simulations have been carried out for a vertical Bridgman crystal growth system for the single crystal growth of NiAl. All three heat transfer modes—conduction, convection and radiation—have been taken into account with reasonable resolutions. A two-level simulation has been performed to simultaneously achieve accuracy as well as computational economy. At the global level, the entire system consisting of the enclosure, heaters and the ampoule have been considered. However, it was desirable to improve the grid resolution within the ampoule to capture the dynamics of the melt/crystal interface. Thus, a refined ampoule simulation was performed using the solution from the Level 1 simulation as the boundary condition for the

Level 2 simulation. This enables an accurate treatment of the solidification dynamics within the ampoule and the heat transfer through the crystal. It is evident that this kind of multi-level approach, with appropriate matching of boundary conditions, is necessary to achieve accuracy at reasonable computing costs.

It has also been shown that variations of the material properties need to be considered in order to achieve a realistic simulation. Significant errors exist for simulations carried out assuming constant material properties. Accurate property data are not readily available in the literature, but have been shown to be necessary to predict the temperature distribution within the crystal growth system.

The predictions reported in the present work are of value in improving our understanding of the growth process and will be of help in controlling the growth parameters in order to achieve the desired melt/crystal interface shape which has implications on the composition and quality of the resulting crystal.

Acknowledgements—This work has been partially supported by AFOSR University Research Initiative Program. Helpful discussions with Drs Mike Kaufmann and Vladimir Levitt of the Materials Science and Engineering Department of the University of Florida are gratefully acknowledged.

REFERENCES

1. S. Sen and D. M. Stefanescu, Melting and casting processes for high-temperature intermetallics, *JOM* **May,** 20–32 (1991).
2. R. Darolia, NiAl alloys for high-temperature structural applications, *JOM* **March,** 44–49 (1991).
3. J. C. Brice, *Crystal Growth Processes*. Blackie, London (1986).
4. R. A. Brown, Theory of transport processes in single crystal growth from the melt, *A.I.Ch.E.J.* **34,** 881–911 (1988).
5. W. Shyy, *Computational Modeling for Fluid Flow and Interfacial Transport*. Elsevier, Amsterdam (1994).
6. F. Rosenberger, *Fundamentals of Crystal Growth*. Springer, New York (1979).
7. M. J. Crochet, F. T. Greyling and J. J. Van Schaftinger, Numerical simulation of horizontal Bridgman growth I: two-dimensional flow, *Int. J. Numer. Meth. Fluids* **7,** 27–49 (1987).
8. M. E. Glicksman, S. R. Coriell and G. B. McFadden, Interaction of flows with the crystal-melt interface, *Ann. Rev. Fluid Mech.* **18,** 307–335 (1986).
9. J. S. Langer, Instabilities and pattern formation in crystal growth, *Rev. Modern Phys.* **52,** 1–28 (1980).
10. H. S. Udaykumar and W. Shyy, Simulation of interfacial instabilities during solidification; part I: conduction and capillarity effects, *Int. J. Heat Mass Transf.* **11,** 2057–2075 (1995).
11. M. J. Kaufman and V. Levit, Private communication (1994).
12. W. Shyy, S. S. Tong and S. M. Correa, Numerical recirculating flow calculation using a body-fitted coordinate system, *Numer. Heat Transfer* **8,** 99–113 (1985).
13. M. E. Braaten and W. Shyy, A study of recirculating flow computation using body-fitted coordinates: consistency aspects and mesh skewness, *Numer. Heat Transfer* **9,** 559–574 (1986).
14. S. V. Patankar, *Numerical Heat Transfer and Fluid Flow*. Hemisphere, Washington, D.C. (1980).
15. V. Voller, Implicit finite-difference solutions of the enthalpy formulation of Stefan problems, *IMA J.* **5,** 201–214 (1985).
16. W. Shyy and M. M. Rao, Enthalpy based formulations for phase-change problems with application to G-jitter, *Microgravity Sci. Tech.* **7,** 41–49 (1994).
17. W. Shyy and M.-H. Chen, Steady-state natural convection with phase change, *Int. J. Heat Mass Transfer* **33,** 2545–2563 (1990).
18. W. Shyy and J. Burke, A study of iterative characteristics of convective–diffusive and conjugate heat transfer problems, *Numer. Heat Transfer* **26B,** 21–37 (1994).
19. R. Siegel and J. R. Howell, *Thermal Radiation Heat Transfer*. Hemisphere, Washington, D.C. (1981).
20. R. H. Perry, D. W. Green and J. O. Maloney (eds), *Perry's Chemical Engineerings' Handbook* (6th Edn). McGraw-Hill, New York (1984).